



Title	Origins of Al-rich chondrules: Clues from a compound Al-rich chondrule in the Dar al Gani 978 carbonaceous chondrite
Author(s)	Zhang, Ai-Cheng; Itoh, Shoichi; Sakamoto, Naoya; Wang, Ru-Cheng; Yurimoto, Hisayoshi
Citation	Geochimica Et Cosmochimica Acta, 130, 78-92 https://doi.org/10.1016/j.gca.2013.12.026
Issue Date	2014-04-01
Doc URL	http://hdl.handle.net/2115/55712
Type	article (author version)
File Information	GCA_130_78-.pdf



[Instructions for use](#)

1
2
3
4
5
6
7
8
9
10
11
12
13
14
15
16
17
18

**Origins of Al-rich chondrules: Clues from a compound Al-rich chondrule
in the Dar al Gani 978 carbonaceous chondrite**

Ai-Cheng Zhang ^{a,b,*}, Shoichi Itoh ^{b,#}, Naoya Sakamoto ^c, Ru-Cheng Wang ^a, and Hisayoshi
Yurimoto ^{b,c}

^a State Key Laboratory for Mineral Deposits Research, School of Earth Sciences and
Engineering, Nanjing University, Nanjing 210046, China

^b Department of Natural History Sciences, Hokkaido University, Sapporo 060-0810, Japan

^c Isotope Imaging Laboratory, Creative Research Institution, Hokkaido University, Sapporo
001-0021, Japan

*Corresponding author. E-mail address: aczhang@nju.edu.cn

#Present address: Division of Earth and Planetary Sciences, Kyoto University, Kyoto 606-
8502, Japan

Revised version to *Geochimica et Cosmochimica acta*

ABSTRACT

Aluminum-rich chondrules are one of the most interesting components of primitive chondrites, because they have characteristics that are similar to both CAIs and ferromagnesian chondrules. However, their precursor and formation history remain poorly constrained, especially with respect to their oxygen isotopic distributions. In this study, we report on the petrography, mineralogy, oxygen isotope ratios, and rare-earth-element compositions of a sapphirine-bearing Al-rich chondrule (SARC) in the ungrouped chondrite Dar al Gani (DaG) 978. The SARC has a complex core-mantle-rim texture; while both the core and the mantle are mainly composed of Al-rich enstatite and anorthite with minor amounts of mesostasis, these regions are distinguished by the presence of Fe-rich spinel and sapphirine in the core and their absence in the mantle. The rim of the SARC consists mainly of Fe-rich olivine, enstatite, and Fe-Ni metal. Spinel and some olivine grains in the SARC are ^{16}O -rich, with $\Delta^{17}\text{O}$ values down to -20‰ and -23‰ , respectively. Enstatite, sapphirine, and most olivine grains have similar $\Delta^{17}\text{O}$ values ($\sim -7\text{‰}$), which are lower than those of anorthite and the mesostasis (including augite therein) ($\Delta^{17}\text{O}$: $\sim -3\text{‰}$). Mesostasis from both the core and mantle have Group II rare-earth-element (REE) patterns; however, the core mesostasis has higher REE concentrations than the mantle mesostasis. These observations provide a strong indication that the SARC formed by the melting and crystallization of a mixture of materials from Group II Ca,Al-rich inclusions (CAIs) and ferromagnesian chondrules. Both spinel and olivine with ^{16}O -rich features could be of relict origin. The ^{16}O -poor isotopic compositions of most components in Al-rich chondrules can be explained by oxygen isotopic exchange between the melt and ^{16}O -poor nebular gas ($\Delta^{17}\text{O}$: $\sim -7\text{‰}$) during melting in chondrule-forming regions; whereas the anorthite and mesostasis could have experienced further oxygen isotopic exchange with a relatively ^{16}O -poor reservoir ($\Delta^{17}\text{O}$: $\sim -3\text{‰}$) on the parent body, likely during fluid-assisted thermal metamorphism. During the same thermal metamorphism event, spinel, olivine, some enstatite, and the mesostasis experienced Mg-Fe exchange to various extents.

INTRODUCTION

49 Aluminum-rich chondrules are defined as round objects in chondrites with igneous
50 textures and high bulk Al_2O_3 contents (≥ 10 wt%; Bischoff and Keil, 1984). They have been
51 observed in most groups of chondrites and have diverse textures and mineralogy (ordinary
52 chondrites, Bischoff and Keil, 1984; Bischoff et al., 1989; Russell et al., 2000; Rubin, 2004;
53 MacPherson and Huss, 2005; enstatite chondrites, Guan et al., 2006; carbonaceous chondrites,
54 Sheng et al., 1991; Krot and Keil, 2002; Krot et al., 2002; Akaki et al., 2007; Zhang and Hsu,
55 2009). The bulk Al_2O_3 contents of Al-rich chondrules are intermediate between those of
56 Ca,Al-rich inclusions (CAIs) and ferromagnesian chondrules (Russell et al., 2005). Because
57 of this compositional feature, Al-rich chondrules can be used to assess possible genetic
58 relationships between CAIs and ferromagnesian chondrules, which are the two main high-
59 temperature crystallization products from the solar nebula preserved in chondritic meteorites.

60 Previous investigations have suggested that Al-rich chondrules could have formed by
61 melting and crystallization of precursor mixtures composed of CAIs and ferromagnesian
62 chondrules (Bischoff and Keil, 1984; Sheng et al., 1991; Krot and Keil, 2002; Krot et al.,
63 2002; MacPherson and Huss, 2005; Zhang and Hsu, 2009), although Rubin (2004) proposed
64 that amoeboid olivine aggregates (AOAs) could also be the precursor materials of some Al-
65 rich chondrules. The key evidence for this conclusion includes high bulk Al_2O_3 contents,
66 relict fragments of CAIs, and fractionated rare-earth-element (REE) patterns (e.g., Misawa
67 and Nakamura, 1988; Sheng, 1992; Krot and Keil, 2002; Krot et al., 2006). In contrast, the
68 oxygen isotopic compositions of most Al-rich chondrules in ordinary and enstatite chondrites
69 ($\delta^{17,18}\text{O}$: ~ -15 to $+5$ ‰; Russell et al., 2000; Guan et al., 2006) are closely related to those of
70 ferromagnesian chondrules (Krot et al., 2006). This led Russell et al. (2000) and Guan et al.
71 (2006) to suggest that Al-rich chondrules were not significantly influenced by remelting of a
72 hybrid mixture of ferromagnesian chondrules and ^{16}O -rich CAI materials, which have $\delta^{17,18}\text{O}$
73 values down to -70 ‰ (Gounelle et al., 2009). However, oxygen isotopic compositions of
74 minerals are subject to resetting during thermal events (e.g., chondrule formation and parent
75 body metamorphism). Therefore, without combining with other geochemical parameters,
76 such as REE patterns, that can be diagnostic of CAIs, it is difficult to determine from these
77 studies alone whether Al-rich chondrules have the same oxygen isotopic compositions as
78 those of their precursors, or have experienced oxygen isotope exchange during melting of
79 their precursors and/or after accretion onto the parent body.

80 The main purpose of this study is to constrain the precursor and formation history of Al-
81 rich chondrules by studying the petrography, mineralogy, bulk composition, and *in situ*
82 oxygen isotopes and REE compositions of a sapphirine-bearing Al-rich chondrule
83 (abbreviated as SARC) with a core-mantle-rim texture from the Dar al Gani (DaG) 978, an
84 ungrouped carbonaceous chondrite (Zhang and Yurimoto, 2013). The combination of REE
85 with oxygen isotope ratios is used as indicators of CAI origin, and diffusion modeling of
86 oxygen and Fe-Mg in minerals is used to constrain thermal history on the parent body.
87 Preliminary results of this study were reported as conference abstracts (Zhang et al., 2011,
88 2013).

89 SAMPLE AND ANALYTICAL METHODS

90 Dar al Gani 978 is a type 3 ungrouped carbonaceous chondrite found in Libya (Choi et
91 al., 2010; Zhang and Yurimoto, 2013). Zhang and Yurimoto (2013) reported detailed
92 petrography and mineralogy of this ungrouped chondrite. Most grains of spinel and olivine in
93 this chondrite are highly FeO-rich. Zhang and Yurimoto (2013) suggested that DaG 978 could
94 have experienced parent-body thermal metamorphism temperature up to 850-950 K.

95 The petrography of the SARC from DaG 978 was studied using scanning electron
96 microscopy (SEM; Hitachi 3400N II) at Nanjing University and field emission-SEM (FE-
97 SEM; JEOL JSM-7000F) at Hokkaido University. Mineral chemistry of the SARC was
98 determined by using electron probe micro-analysis (EPMA; JEOL 8100) at Nanjing
99 University. The operating conditions employed for EPMA measurements were 15 kV
100 accelerating voltage, 20 nA beam current, and a beam size of 1-2 μm . Natural and synthetic
101 standards were used. The typical detection limits for oxides of most elements were better than
102 0.02 wt%. EPMA data were reduced using the ZAF correction procedure.

103 Bulk compositions of the core and mantle in the SARC and their respective mesostasis,
104 were obtained using FE-SEM following the procedure of Zhang and Hsu (2009) under the
105 analytical mode for irregularly outlined materials of the Point&ID Navigator in the X-ray
106 spectroscopy (EDS; Oxford-INCA) system. The energy dispersive spectrometer scans a
107 selected area and outputs the average results of elements in the selected area. Spinel and
108 anorthite grains in sapphirine-bearing objects were used as standards for Si, Mg, Fe, Ca, Al,
109 Cr, Na, and Ti with 100 s counting time; the compositions of these spinel and anorthite grains
110 were previously measured by EPMA, and have confirmed homogeneous compositions among
111 different grains.

112 Oxygen isotopic compositions of minerals in the SARC were measured using the
113 Cameca IMS-1270 instrument at Hokkaido University. The primary ion beam was mass
114 filtered positive Cs^+ ions of 20 keV and the beam spot size was $\sim 3 \mu\text{m}$ in diameter. A
115 primary beam current of $\sim 20 \text{ pA}$ was used to obtain a count rate of negative ^{16}O ions of \sim
116 1×10^7 cps. A normal-incident electron gun was utilized for charge compensation of the
117 sputtered area. Negative ^{16}O ions were detected with an axial Faraday cup, while negative ^{17}O ,
118 ^{16}OH , and ^{18}O ions were detected with an axial electron multiplier, in magnetic peak jumping
119 mode. A mass resolving power of ~ 5500 was used to separate ^{17}O from ^{16}OH . The
120 instrumental mass fractionation effect was corrected using terrestrial spinel, anorthite, olivine,
121 and augite standards (Yurimoto et al., 1994; Katayama et al., 2012; Kawasaki et al., 2012;
122 Wakaki et al., 2013). The reported uncertainties of the individual analyses are expressed in 2σ ,
123 which were estimated by considering both the internal error of each measurement and the
124 reproducibility of the standard measurements. After the measurements, all spots were
125 evaluated using FE-SEM. Data from spots that overlapped undesirable minerals and/or cracks
126 were rejected.

127 The REE concentrations of mesostasis in the SARC were determined with the Cameca
128 IMS-6f instrument at Hokkaido University. The procedure was similar to that described in
129 Yurimoto et al. (1989) and Wang and Yurimoto (1993). The primary beam was mass filtered
130 $^{16}\text{O}^-$ of 14.5 keV and irradiated on the sample surface to a diameter of $\sim 30 \mu\text{m}$. Kinetic
131 energy filtering was achieved by offsetting the sample acceleration voltage (-60 eV) while
132 keeping the electrostatic analyzer voltage, as well as the width and position of the energy slit,
133 constant. The energy bandwidth was 20 eV. The exit slit was set to a mass resolving power of
134 ~ 500 . Positive secondary ion intensities were counted, typically for 10 s, using the peak
135 jumping mode. Each analysis included 20 cycles. Relative sensitivity factors between
136 secondary ion intensity and concentration for each REE (relative to Si) were determined
137 using the Takashima augite, for which REE contents have been well determined by
138 instrumental neutron activation analysis (INAA) (Onuma et al., 1968).

139 RESULTS

140 Petrography and mineralogy of the SARC

141 The sapphirine-bearing Al-rich chondrule from DaG 978 has a round shape of
142 approximately 1.5 mm in diameter. It has a complex core-mantle-rim texture (Fig. 1) based
143 on the change of constituent minerals.

144 The core is approximately 700 μm in diameter and consists mainly of anhedral to
145 euhedral enstatite and anorthite. The enstatite crystals contain thin and parallel cracks
146 perpendicular to the elongate **c**-axis (Fig. 2a). These parallel cracks could have formed during
147 the transformation from high-temperature protoenstatite into clinoenstatite (Yasuda et al.,
148 1983). The most important characteristics of the core are the dense distribution of fine-
149 grained spinel ($<10 \mu\text{m}$) and the presence of euhedral sapphirine in the mesostasis (Fig. 2a).
150 The subhedral to euhedral spinel grains are enclosed not only by Al-rich enstatite and
151 anorthite, but also by euhedral sapphirine (Fig. 2b). Sapphirine occurs mainly in the
152 mesostasis (Fig. 2b). Besides sapphirine and spinel, the mesostasis in the core contains very
153 fine-grained high-Ca pyroxene and anorthite (Fig. 2b). The spinel is FeO-rich, with Mg#
154 values [=mol. % $\text{MgO}/(\text{MgO}+\text{FeO})$] of 58-60 (Table 1). The anorthite has a composition of
155 $\text{An}_{87}\text{-An}_{89}$. Most Al-rich enstatite grains in the core contain low Fs and Wo components
156 ($\text{En}_{96.5-98.0}\text{Fs}_{0.6-2.1}\text{Wo}_{1.4}$) and have high Al_2O_3 contents ($\sim 11.0 \text{ wt}\%$). The sapphirine has a
157 composition close to its stoichiometry ($\text{Mg}_2\text{Al}_4\text{SiO}_{10}$) and contains low FeO (0.39-0.51 wt%).
158 Its TiO_2 and Cr_2O_3 contents are 1.44-1.75 wt% and 1.09-1.42 wt%, respectively (Table 1).
159 EDS results for the average compositions of the bulk core and its mesostasis are given in
160 Table 2. Both the bulk core and its mesostasis have high average contents of Al_2O_3 (29.3 and
161 27.2 wt%, respectively) and FeO (5.4 and 4.6 wt%, respectively). The average Na_2O contents
162 in the bulk core and its mesostasis are both 1.1 wt% (Table 2).

163 The mantle of the SARC is approximately 400 μm thick and is mainly composed of Al-
164 rich enstatite, anorthite, and mesostasis (Fig. 3a). The core and the mantle are distinguished
165 by the presence of spinel (core) and the lack of spinel (mantle) in the mineral assemblage (Fig.
166 3b). Unlike their counterparts in the core, Al-rich enstatite and anorthite in the mantle are
167 coarser-grained (Fig. 3a), with some anorthite grains that are approximately 60 μm wide.
168 Most Al-rich enstatite grains also contain thin and parallel cracks perpendicular to the **c** axis,
169 whose formation could be related to the transformation from high-temperature protoenstatite
170 into clinoenstatite. The mesostasis in the mantle consists mainly of relatively coarse-grained
171 high-Ca pyroxene (up to 20 μm in diameter) and anorthite than those in the core mesostasis.
172 Chemically zoned and Al-poor enstatite grains often occur in or adjacent to mesostasis in the
173 mantle (Fig. 3c). It is noteworthy that some anhedral to subhedral olivine grains and FeNi
174 metals (10-60 μm in size) occur locally in the mantle, close to the margin of this chondrule
175 (Fig. 3d). Anorthite grains in the mantle contain slightly lower An components (An_{82-87}) than
176 those in the core of the SARC (Table 1). Most coarse Al-rich enstatite grains ($\text{En}_{97.7-97.9}\text{Fs}_{0.6-}$

177 $_{0.8}\text{Wo}_{1.4-1.6}$) contain high Al_2O_3 (8.13-10.7 wt%) and low FeO (0.37-0.50 wt%) (Table 1).
178 However, the zoned enstatite grains ($\text{En}_{77.4-97.6}\text{Fs}_{1.1-21.2}\text{Wo}_{0.8-1.7}$) in and adjacent to mesostasis
179 contain lower Al_2O_3 (3.71-7.11 wt%) and higher FeO (0.73-14.0 wt%). The high-Ca
180 pyroxene grains ($\text{En}_{31.6-48.5}\text{Fs}_{17.6-18.5}\text{Wo}_{34.0-50.7}$) in the mantle mesostasis are FeO-rich
181 ($\text{Mg}\#=64.1-73.4$) and have large variations in Al_2O_3 and TiO_2 contents (0.43-4.91 and 0.14-
182 3.06 wt%, respectively). Olivine in the mantle is FeO-rich ($\text{Mg}\#=68.1-71.2$). The average
183 bulk compositions of the mantle and its mesostasis are also given in Table 2. Compared to the
184 bulk core and its mesostasis, the bulk mantle and its mesostasis have higher average amounts
185 of SiO_2 and CaO and lower average amounts of MgO and Al_2O_3 (Table 2). The bulk mantle
186 and its mesostasis contain high FeO (4.5 and 6.6 wt%, respectively) and Na_2O (1.8 and 1.7
187 wt%, respectively).

188 The rim of the SARC is mainly composed of olivine, enstatite, and Fe-Ni-metal and
189 occurs discontinuously (Figs. 1 and 4a). A few fine and irregular grains of anorthite are
190 present in the rim; however, no apparent mesostasis was observed. At some sections, the
191 olivine-enstatite assemblages are partially enclosed in the mantle (Fig. 4b). The texture and
192 mineralogy of the rim, with round-shaped olivine and FeNi metal grains enclosed by enstatite,
193 are almost the same as those of porphyritic olivine-pyroxene chondrules observed in DaG
194 978 (Zhang and Yurimoto, 2013). Olivine in the rim is also Fe-rich ($\text{Mg}\#=68.7-69.3$) and is
195 almost identical in composition to olivine in the mantle (Table 1). Enstatite grains ($\text{En}_{74.0-}$
196 $_{92.6}\text{Fs}_{6.5-24.3}\text{Wo}_{0.9-1.7}$) in the rim are usually low in Al_2O_3 (~ 1 wt%) and have a large variation
197 in $\text{Mg}\#$ (75.3-93.4).

198 **Oxygen isotopic compositions of the SARC**

199 Minerals in the SARC have a large variation in oxygen isotopic composition (Table 3)
200 and almost all data lie along the carbonaceous chondrite anhydrous minerals (CCAM) line
201 (Fig. 5).

202 The oxygen isotopic compositions of more than ten spinel grains from the core of the
203 SARC were measured. However, nine of the ten measurements, that show ^{16}O -enrichments to
204 various degrees, were contaminated by surrounding minerals or cracks due to the small spinel
205 grain sizes and were rejected. One spinel grain was successfully measured without
206 contamination from surrounding minerals and cracks, and the result indicated ^{16}O -enrichment
207 ($\Delta^{17}\text{O} = -19.9\text{‰}$; Table 3). Sapphirine in the core mesostasis of the SARC has a small grain-
208 to-grain variation in $\Delta^{17}\text{O}$ from -7.7 to -5.8‰ (Fig. 5; Table 3). The Al-rich enstatite grains in

209 the core of the SARC have oxygen isotopic compositions ($\Delta^{17}\text{O} = -7.5$ to -3.7‰) similar to
210 those of sapphirine. Anorthite from the core of the SARC is ^{16}O -poor (Table 3; Fig. 5) and
211 has a small variation of oxygen isotopic compositions ($\Delta^{17}\text{O} = -4.6$ to -2.7‰). The core
212 mesostasis (not overlapping sapphirine) has oxygen isotopic compositions ($\Delta^{17}\text{O} = -4.2$ to $-$
213 1.0‰) similar to those of anorthite.

214 Aluminum-rich enstatite in the mantle of the SARC has oxygen isotopic compositions
215 ($\Delta^{17}\text{O} = -8.8$ to -3.8‰) similar to those in the core of the SARC. Oxygen isotopic
216 compositions of anorthite ($\Delta^{17}\text{O} = -4.7$ to 0.2‰) and mesostasis (including a $20\text{-}\mu\text{m}$ -size
217 augite grain @95 therein shown in Fig. 3c) ($\Delta^{17}\text{O} = -3.3$ to -0.6‰) in the mantle are also
218 similar to those in the core of the SARC, respectively. Oxygen isotopic compositions of most
219 olivine grains ($\Delta^{17}\text{O} = -8.8$ to -3.8‰) in the mantle are similar to those of Al-rich enstatite
220 (Table 3; Fig. 5); however, one analysis (@46, which is in the same olivine#1 grain with @49
221 and @51) shows a ^{16}O -rich oxygen isotopic composition with the $\Delta^{17}\text{O}$ value down to $-$
222 11.6‰ (Table 3).

223 Enstatite in the rim of the SARC has oxygen isotopic compositions ($\Delta^{17}\text{O} = -8.2$ to $-$
224 6.6‰) generally similar to those in the core and the mantle. Differing from enstatite, olivine
225 in the rim of the SARC has a large variation of oxygen isotopic composition among different
226 grains, with $\Delta^{17}\text{O}$ varying from -23.0‰ to -4.5‰ . Similar to those in olivine#1 grain,
227 variable oxygen isotopic compositions within a few single olivine grains were observed (e.g.,
228 spots @132, @133, and @135 in olivine#3 grain; Table 3). However, based on the few
229 measured spots of single olivine grains, it is difficult to determine whether there is gradual
230 zoning of the oxygen isotopic compositions.

231 In summary, spinel and some olivine grains in the SARC are ^{16}O -rich, with $\Delta^{17}\text{O}$ down
232 to -19.9‰ and -23.0‰ , respectively. Al-rich enstatite, sapphirine, enstatite, and most olivine
233 grains have oxygen isotopic compositions similar to each other ($\Delta^{17}\text{O}$: $\sim -7\text{‰}$). Meanwhile,
234 anorthite and mesostasis (including the $20\text{-}\mu\text{m}$ -size augite therein) have similar oxygen
235 isotopic compositions and are even more ^{16}O -poor ($\Delta^{17}\text{O}$: $\sim -3\text{‰}$) than those of Al-rich
236 enstatite, sapphirine, enstatite, and most olivine grains.

237 **Rare-earth-element compositions of mesostasis**

238 Analytical results for REE in eight mesostasis samples from the core and the mantle of
239 the SARC are given in Table 4 and the CI-normalized abundances of the REEs are plotted in

240 Fig. 6 (Anders and Grevesse, 1989). Both mesostasis in the core and mantle are enriched in
241 REE and have Group II REE patterns with a flat light REE (LREE) pattern and a fractionated
242 heavy REE (HREE) pattern (Fig. 6). However, the REE abundances of the core mesostasis
243 (La $\sim 102\text{-}157 \times \text{CI}$) are higher than those of the mantle mesostasis (La $\sim 65\text{-}132 \times \text{CI}$; Fig. 6).

244

DISCUSSION

245 Precursor materials and melting environment of the Al-rich portion in the SARC

246 The precursor materials of an Al-rich chondrule are one of the key constraints to its
247 origin. Previous investigations have suggested that some Al-rich chondrules are related to a
248 mixture of CAIs and ferromagnesian chondrules, based on the bulk chemistry, the presence of
249 relict fragments of CAIs, and fractionated REE patterns (e.g., Sheng, 1992; Russell et al.,
250 2000; Krot and Keil, 2002; Krot et al., 2002; MacPherson and Huss, 2005; Zhang and Hsu,
251 2009). However, oxygen isotopic compositions ($\delta^{17,18}\text{O}$: ~ -15 to $+5$ ‰) of minerals in Al-
252 rich chondrules from ordinary chondrites (Russell et al., 2000) and enstatite chondrites (Guan
253 et al., 2006) are closely related to those of ferromagnesian chondrules. These results led them
254 to suggest that the precursor materials of Al-rich chondrules are not simple mixtures of
255 materials from CAIs and ferromagnesian chondrules (e.g., Russell et al., 2000; Guan et al.,
256 2006). In this section, we will discuss our observations with respect to the possibility that the
257 precursor materials of the Al-rich core and mantle in SARC are mixtures of materials from
258 CAIs and ferromagnesian chondrules.

259 First, the Al-rich portion (including the core and the mantle) of the SARC has
260 intermediate bulk chemistry and mineralogy between those of CAIs and ferromagnesian
261 chondrules. On one hand, both the core and mantle of the SARC contain much higher Al_2O_3
262 (up to 29 wt%), relative to the amount in ferromagnesian chondrules. This is due to the
263 dominance of Al-rich minerals (spinel, anorthite, and Al-rich pyroxene) in the core and
264 mantle of the SARC. On the other hand, the core and mantle have lower CaO contents than
265 typical CAIs, which are due to the presence of low-Ca pyroxene, rather than high-Ca
266 pyroxene in SARC core and mantle. Olivine and FeNi-metal, the common minerals of
267 ferromagnesian chondrules, are also present in the mantle. Thus, the petrography, bulk
268 compositions, and mineralogy support that the precursor material of the Al-rich portion (core
269 and mantle) of the SARC is a mixture of materials from CAIs and ferromagnesian chondrules.

270 Second, mesostasis from both the core and mantle of the SARC have REE patterns
271 similar to those of Group II refractory inclusions. The Group II REE pattern is usually
272 explained by fractional removal of some ultra-refractory elements, which could have
273 concentrated in early condensed solids from a nebula (Boynton, 1975; Davis and Grossman,
274 1979; Palme et al., 1982). This REE pattern is only consistent with an origin of refractory
275 inclusions, although it does not occur in all refractory inclusions. Thus, although the REE
276 patterns of the bulk Al-rich portion in the SARC could be slightly different from those of
277 mesostasis, due to the igneous fractionation of pyroxene and anorthite, REE pattern should
278 still be similar to that of Group II refractory inclusions because REEs are incompatible in
279 anorthite and enstatite; therefore REEs should be concentrated in mesostasis. The Al-rich
280 portion of the SARC contains very minor amounts of olivine, so that it seems unlikely that
281 amoeboid olivine aggregate (AOA) precursor material is a main contributor to the precursor
282 materials of the Al-rich portion in SARC. Thus, the REE patterns of mesostasis from the core
283 and mantle strongly suggest that the precursor materials of the Al-rich portion in the SARC
284 are related to materials from Group II CAIs.

285 Third, it is well accepted that primitive refractory inclusions are ^{16}O -rich, whereas
286 chondrules are usually ^{16}O -poor (Yurimoto et al., 2008). Of course, in the literature (e.g.,
287 Maruyama et al., 1999; Yurimoto and Wasson, 2002; Maruyama and Yurimoto, 2003; Jones et
288 al., 2004; Nagashima et al., 2012), there are a few reports that some minerals in chondrules
289 also have ^{16}O -rich oxygen isotopic compositions. However, most of these investigators
290 suggested that the ^{16}O -rich features could be related to relict materials from Ca,Al-rich
291 inclusions or amoeboid olivine aggregates. Alternatively, Jones et al. (2004) also proposed
292 that the earliest nebular solids from which chondrules formed are ^{16}O -rich as discussed by
293 Kobayashi et al. (2003), since no petrographic and mineralogical supporting a relict origin
294 from refractory inclusions was observed in their study. In this study, we favor that the ^{16}O -
295 rich feature of the spinel in the SARC is additional evidence that supports the precursor
296 material of the core in the SARC is related to materials from CAIs.

297 Thus, it is concluded that the precursor of the Al-rich portion in the SARC must have
298 been a mixture of materials from CAIs with a Group II REE pattern and ferromagnesian
299 chondrules. The materials from CAIs should be dominant in the mixture. We can also infer
300 that the minerals (e.g., Al-rich enstatite and sapphirine) crystallized from in the Al-rich
301 portion of the SARC were more ^{16}O -rich than those of the minerals crystallized from
302 ferromagnesian chondrules (e.g., enstatite and most olivine grains in the rim of the SARC)

303 and those of the ferromagnesian chondrule components in most chondrites (e.g., Krot et al.,
304 2006; Yurimoto et al., 2008; Ushikubo et al., 2012; Tenner et al., 2013). Instead, in contrast to
305 this inference, the oxygen isotope compositions of Al-rich enstatite and sapphirine in the
306 SARC are similar to those of enstatite and most olivine grains in the rim. This observation is
307 similar to those from previous investigations (Russell et al., 2000; Guan et al., 2006). It is
308 very likely that the oxygen isotopic compositions of most minerals in the Al-rich portion of
309 the SARC had been reset during melting of the Al-rich portion of the SARC precursor
310 materials and/or after accretion into the parent body. In this study, we suggest that the oxygen
311 isotopic compositions of most minerals crystallized from the Al-rich portion of the SARC
312 (except the ^{16}O -rich spinel) had been reset during the heating and melting event of their
313 precursor materials in the nebula; whereas the oxygen isotopic compositions of anorthite and
314 mesostasis were further modified on the parent body. In addition, the ferromagnesian
315 components (including the rim and olivine and metal in the mantle) in the SARC could have
316 formed in a separate process (will be discussed in detail later on), which is not related to the
317 precursor materials of the Al-rich portion of the SARC and their melting.

318 Yu et al. (1995) performed high-temperature oxygen isotopic exchange experiments,
319 which indicated that oxygen isotopic compositions between a chondrule analogue melt and
320 water vapor could reach equilibrium on a scale of minutes. Therefore, if the precursor
321 materials of the Al-rich portion in the SARC were melted, the melt could readily approach
322 oxygen isotopic equilibrium with the surrounding ^{16}O -poor nebular gas. Meanwhile, the ^{16}O -
323 rich spinel could be of relict origin during melting of the precursor. The self-diffusion speed
324 of oxygen in solid spinel is very slow (Ryerson and McKeegan, 1994). At 1400 K, an oxygen
325 diffusion length of 1 μm in spinel could require ~ 170 years, which is much longer than the
326 duration of high temperature in chondrule-forming events (probably tens of hours, Desch et al.
327 2012). Thus, it is reasonable that relict spinel can retain its ^{16}O -rich feature during the
328 chondrule-forming event, while minerals crystallized from the melt adopt ^{16}O -poor features
329 ($\Delta^{17}\text{O}$: $\sim -7\%$) due to melt-gas oxygen isotopic exchange in the nebula. The similarity
330 between oxygen isotopic compositions of Al-rich enstatite and sapphirine in the SARC and
331 those of ferromagnesian chondrule materials from other chondrites (e.g., Krot et al., 2006;
332 Yurimoto et al., 2008; Ushikubo et al., 2012; Tenner et al., 2013) also supports this inference.

333 **Crystallization of the Al-rich core and mantle in the SARC**

334 The ferromagnesian rim in SARC has a distinctly different texture and mineral
335 assemblages, relative to those of the Al-rich portion in the SARC. Ferromagnesian

336 components in the rim, as well as Fe-rich olivine in the mantle, were probably attached onto
337 the mantle of SARC during solidification of the mantle. Their formation will be discussed
338 separately in the following section. In this section, we focus mainly on the crystallization of
339 the Al-rich portion in the SARC. The boundary between the core and mantle of the SARC
340 implies three possible interpretations for the core-mantle texture of the Al-rich portion: 1) The
341 core and mantle may have formed during two heating/melting events in the nebula (e.g.,
342 Akaki et al., 2007). 2) The core and mantle formed under a single heating/melting event in
343 the nebula and crystallization proceeded from the mantle to the core. 3) The core and mantle
344 formed under a single heating/melting event in the nebula and crystallization proceeded from
345 the core to the mantle.

346 Akaki et al. (2007) studied a compound Al-rich chondrule from Allende, which also
347 contains distinct textural domains. They proposed a model of two heating/melting events to
348 interpret the texture and oxygen isotopic distribution of olivine in that Al-rich chondrule. In
349 the model, the core, which is considered as the primary chondrule, was formed during the
350 first heating/melting event, and the mantle was then formed by the melting of core
351 plagioclase and a porous dust clump that surrounded the primary chondrule. For the case of
352 the SARC, this model can explain the decrease in the REE concentrations of mesostasis from
353 the core to the mantle, assuming that the dust clump is REE-poor. However, this model may
354 have difficulty in explaining the presence of sapphirine in the core. Crystallization
355 experiments conducted by Sheng (1992) suggested that sapphirine is a metastable phase in
356 Al-rich chondrules. Thus, if the core was reheated to ~ 1260 °C, sapphirine would likely have
357 disappeared from the phase assemblage. In this study, we observed that most Al-rich enstatite
358 grains in the core and mantle of the SARC are clinoenstatite that transformed from high-
359 temperature protoenstatite, based on their parallel cracks perpendicular to the *c* axis (Yasuda
360 et al., 1983). This indicates that, at a minimum, both the core and mantle crystallized above
361 1000 °C (Yasuda et al., 1983). If the temperature were significantly higher, sapphirine would
362 have disappeared during a second heating/melting event, which is clearly inconsistent with its
363 presence in the core. Thus, it is unlikely that the core and mantle of the SARC were formed
364 by two separate heating/melting events.

365 The model that the core and mantle of the SARC formed under a single heating/melting
366 event is supported by the similarity of REE patterns of the core and mantle mesostasis,
367 especially one of the REE analyses of the mantle mesostasis overlaps with those of the core
368 mesostasis. Meanwhile, the variation of REE concentrations in the mesostasis would also be

369 a powerful indicator of the crystallization sequence. Anorthite and enstatite are the major
370 components in the Al-rich portion of the SARC and are incompatible for REEs; therefore, the
371 REE concentrations of the melt should tend to increase with the fractionation of anorthite and
372 enstatite during crystallization. Also fractionation of primary anorthite during crystallization
373 would cause deeper negative Eu anomaly of core mesostasis vs. mantle mesostasis. Therefore,
374 the variation of REE concentrations of the mesostasis supports that the crystallization
375 proceeded from the mantle to the core (e.g., Fig. 6). This conclusion is also consistent with
376 the euhedral shape and large grain sizes of most anorthite and enstatite in the mantle; whereas
377 the anhedral to euhedral shape and small grains of anorthite and enstatite in the core could be
378 due to space limitations during crystallization. The slightly lower An value of anorthite in the
379 mantle could be due to a higher degree of secondary sodium-metasomatism in the mantle,
380 relative to that in the core. The slightly higher Na₂O content in mesostasis of the mantle,
381 relative to that of the core also supports this interpretation. However, this crystallization
382 sequence (from the mantle to the core) seems to conflict with the presence of relict spinel,
383 because relict spinel grains are the preferred nucleation sites if there is no significant
384 temperature gradient between the core and the mantle.

385 If the crystallization of the Al-rich portion started from the core by nucleation on relict
386 spinel, then the variation of the anorthite An values from the core to the mantle is consistent
387 with the crystallization sequence, meaning that no secondary sodium-metasomatism was
388 required. However, to explain the relatively low REE concentrations of the mantle mesostasis,
389 when compared to those from the core, would require the addition of REE-poor material
390 during crystallization of the mantle. The olivine and FeNi-metal could represent this REE-
391 poor material; however, the minor amount of olivine and FeNi-metal observed in the mantle
392 of the SARC does not seem sufficient to explain the dilution effect of REE in the mantle.

393 Based on the discussion above, melting under a single heating/melting event and
394 crystallization that proceeded from the mantle to the core seems to be the most likely scenario
395 for the formation and crystallization of the Al-rich portion in the SARC. This single stage
396 heating event model is also consistent with the almost same oxygen isotopic compositions of
397 Al-rich enstatite from the core and the mantle; chondrules formed during heating events at
398 different local regions may preserve various primary oxygen isotopic compositions
399 (Ushikubo et al., 2012). The different bulk composition and mineralogy in mesostasis from
400 the core and mantle could be due to the formation separate melt pockets during crystallization
401 of enstatite and anorthite.

402 Tronche et al. (2007) have performed experiments to understand the effects of bulk
403 compositions, peak temperatures, and cooling rates on the mineralogy and texture of Al-rich
404 chondrules. They concluded that the textures of anorthite-rich compositions are more
405 sensitive to peak temperatures than they are to cooling rates. In their run products, higher
406 peak temperatures response to coarser textures; meanwhile, at the same peak temperatures,
407 slower cooling rates lead to lower aspect ratios of anorthite laths. For the case of the Al-rich
408 portion of the SARC, which is anorthite-rich (Fig. 1), the sizes of anorthite laths in the mantle
409 are comparable to those of run products cooled from a peak temperature of 1475 °C (Tronche
410 et al., 2007) and are much coarser than those of experiments cooled from a peak temperature
411 of 1401 °C and 1452 °C (Tronche et al., 2007). And, the aspect ratios of anorthite grains are
412 comparable to those of run products cooled at 5-10 °C/h. This indicates that the mantle of the
413 SARC could have crystallized from a peak temperature between 1452-1475 °C and at cooling
414 rates of 5-10 °C/h. In addition, as pointed out by Sheng (1992), sapphirine is a metastable
415 phase during crystallization and not stable at 1253-1260 °C. Therefore, the presence of
416 sapphirine in the core mesostasis implies that the core could have completed its
417 crystallization below 1253 °C. This inference is consistent with the various textures of run
418 products cooled from different peak temperatures (Tronche et al., 2007).

419 **Formation of ferromagnesian components in the SARC**

420 The ferromagnesian components in the SARC include the chondrule-like rim, and
421 olivine and FeNi metal grains observed in the mantle. The olivine grains in the mantle have
422 similar petrographic, mineralogical, and oxygen isotopic features to those in the rim, which
423 suggests that the ferromagnesian components in the mantle and the rim have a common
424 origin.

425 All olivine grains in the SARC have sub-rounded to rounded shapes and all olivine
426 grains in the rim are embedded in enstatite. This feature is similar to that of most porphyritic
427 olivine-pyroxene chondrules (Zhang and Yurimoto, 2013), which implies similar formation
428 processes. Most olivine grains have ¹⁶O-poor oxygen isotopic compositions similar to that of
429 enstatite, which is also a typical feature of porphyritic olivine-pyroxene chondrules from
430 unmetamorphosed carbonaceous chondrites (Ushikubo et al. 2012; Tenner et al., 2013).
431 Therefore, the oxygen isotopic compositions of enstatite may represent those of the
432 chondrule-forming region. Interestingly, a few olivine grains are ¹⁶O-rich to various degrees.
433 Similar ¹⁶O-rich isotopic compositions in chondrule olivine have also been previously
434 reported (e.g., Hiyagon and Hashimoto, 1999; Jones et al., 2004; Nagashima et al., 2012;

435 Ushikubo et al., 2012; Tenner et al., 2013) and are likely of relict origin, although Jones et al.
436 (2004) also proposed an alternative interpretation that the earliest nebular solids from which
437 chondrules formed had $\delta^{17}\text{O}$ and $\delta^{18}\text{O}$ values around -50‰ . The relict origin for these olivine
438 grains could be similar to the origin of the ^{16}O -rich spinel discussed earlier or of the ^{16}O -rich
439 olivine of a ^{16}O -rich chondrule (Kobayashi et al., 2003), as both phases have similarly slow
440 oxygen diffusion rates under chondrule-forming conditions (Ryerson et al., 1989; Ryerson
441 and McKeegan, 1994). The ^{16}O -rich olivine in the SARC could also be of relict origin due to
442 incomplete melting during the chondrule-forming event (not the event that caused melting of
443 the precursor of the Al-rich portion in SARC). Analyses that indicate intermediate $\Delta^{17}\text{O}$
444 probably reflect various contributions from ^{16}O -rich (e.g., $\Delta^{17}\text{O} = -23\text{‰}$) and ^{16}O -poor (e.g.,
445 $\Delta^{17}\text{O} = -7\text{‰}$) domains within each measurement spot. However, one olivine grain in the
446 SARC has an extremely low $\Delta^{17}\text{O}$ (-23‰) that is almost identical to that of olivine in pristine
447 CAIs and AOAs (Hiyagon and Hashimoto, 1999; Komatsu et al., 2001; Yurimoto and Wasson,
448 2002; Imai and Yurimoto, 2003; Itoh et al., 2004; Itoh et al., 2007). In addition, olivine grains
449 from DaG 978 AOA have similar CaO contents (<0.1 wt%) to those in the SARC (Zhang and
450 Yurimoto, 2013), and both are lower in CaO contents than olivine from CAIs (CaO >0.1 wt%)
451 in the same sample (Zhang and Yurimoto, 2013). This indicates that the ^{16}O -rich feature of
452 some olivine grains in the SARC could have been derived from AOAs.

453 **Post-crystallization processes in the SARC**

454 One post-crystallization process recorded in SARC involves iron-enrichment in the
455 oxide and silicate minerals. For example, enstatite along cracks and grain boundaries is FeO-
456 enriched, which indicates that Fe-Mg interdiffusion occurred after the crystallization of
457 enstatite. This interpretation is supported by the fact that sapphirine and most enstatite (Al-
458 rich and Al-poor) grains in the SARC are FeO-poor, with Mg# values up to 99, suggesting
459 that they initially formed in a FeO-depleted system. Spinel and olivine are also FeO-rich
460 (Mg#: ~ 60 and 70 , respectively) and are highly unequilibrated with FeO-poor enstatite. The
461 Mg# values of spinel and olivine are instead similar to those of other grains of spinel and
462 olivine from DaG 978 (Zhang and Yurimoto, 2013). Therefore, the FeO-rich features of
463 spinel and olivine indicate secondary processes involving Mg-Fe exchange in the oxides and
464 silicates, probably due to thermal metamorphism on the parent body. Zhang and Yurimoto
465 (2013) suggested that the metamorphic temperature on the parent body of DaG 978 could be
466 up to 850-950 K, based on spinel-olivine geothermometric calculations.

467 The other post-crystallization process recorded in the SARC involves the exchange of
468 oxygen isotopes in anorthite and mesostasis (including a relatively coarse mesostasis augite
469 grain up to 20 μm in size). The Al-rich portion in the SARC has an igneous texture; therefore,
470 its components, except for relict spinel, should have nearly identical $\Delta^{17}\text{O}$ (c.f., Ushikubo et
471 al., 2012). However, the present data indicate that anorthite and mesostasis (very fine-grained
472 augite and anorthite/glass therein) have higher $\delta^{18}\text{O}$ and $\Delta^{17}\text{O}$ than enstatite, olivine, and
473 sapphirine. This oxygen isotopic difference cannot be explained by melt-gas oxygen isotopic
474 exchange during crystallization of the SARC, because the oxygen isotopic distribution in
475 different minerals is not correlated with their crystallization sequence. For instance,
476 sapphirine in mesostasis and enstatite have similar $\Delta^{17}\text{O}$ values that are lower than those of
477 anorthite and mesostasis. Oxygen usually has faster diffusion rates in anorthite and
478 mesostasis when compared to in pyroxene, olivine, and spinel (Ryerson et al., 1989; Ryerson
479 and McKeegan, 1994); therefore, it is likely that the high $\Delta^{17}\text{O}$ of anorthite and mesostasis in
480 the SARC is due to secondary oxygen isotope exchange after the solidification of the SARC
481 (e.g., Wasson et al., 2001; Krot et al., 2008; Rudraswami et al., 2011). In addition, it is also
482 possible that oxygen isotopic exchange in both anorthite and mesostasis, as well as the Mg-Fe
483 exchange in minerals in the SARC, occurred during the same thermal metamorphic event on
484 the parent body.

485 To further evaluate the feasibility of and conditions for O-isotope and Fe-Mg exchange
486 on the parent body of DaG 978, the diffusion of oxygen and Fe-Mg in different minerals
487 under anhydrous and hydrous conditions was calculated based on elemental diffusion
488 coefficients for different minerals available in the literature and with various assumptions
489 (Giletti et al., 1978; Freer and O'Reilly, 1980; Hallwig et al., 1982; Jaoul et al., 1983; Elphick
490 et al., 1988; Farver, 1989; Ryerson et al., 1989; Ryerson and McKeegan, 1994; Hier-
491 Majumder et al. 2005; Chakraborty, 2010). The minimum temperatures and durations (solid
492 curves in Fig. 7) are constrained according to the estimated oxygen and Fe-Mg diffusion
493 lengths in various minerals (30 and 10 μm for oxygen diffusion in anorthite and augite,
494 respectively; 5, 15, 10, and 5 μm for Fe-Mg interdiffusion in spinel, olivine, augite, and in Al-
495 poor enstatite, respectively).

496 The required diffusion temperatures and durations (dashed curves in Fig. 7) were also
497 calculated for 1 μm diffusion of oxygen in spinel and olivine. These diffusion temperatures
498 and durations likely represent upper limits because no oxygen isotopic compositions of spinel

499 and olivine were observed to be similar to those of anorthite and mesostasis, even if spinel
500 and olivine were measured near the grain boundaries.

501 Diffusion calculations under anhydrous conditions (Fig. 7a) have two major implications.
502 First, for a given temperature and time duration, the diffusion distance of oxygen in anorthite
503 is approximately twice the distance of Fe-Mg interdiffusion in forsterite. This suggests that
504 the oxygen isotopic composition of anorthite was changed when the Mg-Fe content of olivine
505 was re-equilibrated during metamorphism on the parent body. However, it is difficult to
506 explain the ^{16}O -poor composition of augite in the mesostasis by oxygen diffusion during the
507 metamorphic event because the required temperature and duration for oxygen diffusion in
508 augite is above those for oxygen diffusion in spinel and olivine (Fig. 7a). One possibility is
509 that the augite is a metamorphic crystal crystallized during the metamorphic event (e.g.
510 Rudraswami et al., 2011).

511 Second, in order to achieve equilibrium of the oxygen isotopic composition in anorthite,
512 as well as the Fe-Mg compositions in spinel, forsterite, and for Fe to penetrate into Al-poor
513 enstatite by diffusion, the estimated diffusion duration is around 1 Myr at a temperature of
514 850-950 K, which seems to be likely for a chondrite with a petrologic type of 3.6 (Zhang and
515 Yurimoto, 2013). Therefore, if the large augite grain with high $\Delta^{17}\text{O}$ (-3‰) in the mesostasis
516 crystallized during thermal metamorphism on the parent body, then it is likely that the oxygen
517 isotopic exchange in anorthite and the Fe-Mg diffusion in spinel, olivine, and enstatite
518 occurred under anhydrous metamorphic conditions.

519 All the diffusion curves measured under aqueous fluid saturated conditions (Fig. 7b)
520 have significant shifts to lower temperatures at a given time duration, when compared with
521 those measured under anhydrous conditions. This indicates that the Mg-Fe and oxygen
522 isotopic exchange in minerals of the chondrule could have occurred easily under some degree
523 of hydrous conditions because the presence of aqueous fluid significantly enhances the
524 diffusion rates of oxygen and Fe-Mg in minerals. However, it should be noted that the
525 diffusion coefficients under water saturated conditions used in Fig. 7 may be too large to
526 constrain the O isotopic exchange of ^{16}O -rich minerals and that the experimental diffusion
527 coefficients have high uncertainties compared with those under anhydrous conditions.
528 Considering the presence of low-temperature alteration products (e.g., secondary nepheline)
529 in DaG 978 (Zhang and Yurimoto, 2013), it is possible that the presence of water during
530 thermal metamorphism under hydrous conditions assisted elemental and isotopic exchange in
531 minerals.

532 **Model for the formation of the SARC and comparison with other Al-rich chondrules**

533 These discussions indicate that the SARC in DaG 978 has experienced multiple
534 formation processes, which involved the mixing and melting of materials from refractory
535 inclusions and ferromagnesian chondrules. The most probable model for the formation of the
536 SARC includes the following stages (Fig. 8). a) Condensation of a CAI from ^{16}O -rich nebular
537 gas ($\Delta^{17}\text{O} < -20\%$) where ultra-refractory components have been removed. This process
538 resulted in the Group II REE pattern of the CAI. b) The Group II CAI was then transported
539 into the chondrule-forming region, where it mixed with ferromagnesian material (that forms
540 chondrule and/or matrix of chondrites). c) The hybrid between the Group II CAI and
541 ferromagnesian material was melted, probably by a heating event related to chondrule-
542 forming events, and experienced oxygen isotope exchange in a ^{16}O -poor chondrule-forming
543 region ($\Delta^{17}\text{O} = -7\%$). Based on the texture comparison between SARC and those of
544 experimental run products by Tronche et al. (2007), the peak crystallization temperature of
545 the Al-rich portion of SARC was likely between 1452-1475 °C. However, in this heating
546 event, spinel grains were not melted and retained their original ^{16}O -rich oxygen isotopic
547 compositions. d) Upon cooling, the Al-rich melt crystallized from the mantle to the core.
548 Some ferromagnesian chondrule materials were attached on the Al-rich melt and some
549 fragments are partly or totally encapsulated in the Al-rich melt. e) After accretion into the
550 parent body of DaG 978, anorthite and mesostasis in the SARC experienced oxygen isotopic
551 exchange with relatively ^{16}O -poor fluid ($\Delta^{17}\text{O}: -3\%$) during fluid-assisted thermal
552 metamorphism; during this process, spinel, olivine, some enstatite, and mesostasis
553 experienced Mg-Fe exchange.

554 Interestingly, two other sapphirine-bearing Al-rich chondrules (USNM 3510 and
555 BG82CLII) and a few previously reported cordierite-bearing Al-rich chondrules (Fuchs, 1969;
556 Sheng et al., 1991; Akaki et al., 2007) also have similarly complex textures and mineral
557 assemblages. All of these sapphirine and cordierite-bearing Al-rich chondrules have complex
558 core-mantle features and their dominant Al-rich minerals are anorthite and Al-rich enstatite,
559 rather than Al-rich diopside. In addition, small spinel grains are typically enclosed by
560 anorthite, Al-rich enstatite, sapphirine or cordierite. The main difference among these
561 complex Al-rich chondrules is the variation in the abundance of primary olivine from these
562 Al-rich melts. The similarity in petrographic texture, mineral assemblage, and even oxygen
563 isotopic composition among these sapphirine-bearing and cordierite-bearing Al-rich
564 chondrules may indicate that they have experienced similar formation processes. The

565 differences in mineralogy between these Al-rich chondrules could be due to variety in the
566 bulk compositions of their precursor materials. Compared to the Al-rich chondrules with
567 complex textures, Al-rich chondrules with simple textures could have experienced high
568 enough temperatures that would have melted all precursor materials, which would have
569 allowed for near-complete oxygen isotope exchange with surrounding nebular gas in
570 chondrule-forming regions. If correct, it could well explain the similarity in the oxygen
571 isotopic compositions of most Al-rich chondrules when compared to those of ferromagnesian
572 chondrules. However, although our oxygen isotope and REE data show that Al-rich
573 chondrules could have formed by melting of hybrid of materials from CAIs and chondrules,
574 some Al-rich chondrules contain no diagnostic evidence for the existence of CAI precursors.
575 For example, MacPherson and Huss (2005) measured trace-element compositions for eleven
576 Al-rich chondrules from unequilibrated ordinary chondrites. And no Group II REE patterns
577 were observed for these 11 Al-rich chondrules. Thus, it suggests that some of these Al-rich
578 chondrules, if not all, cannot be explained by the hybrid model inferred from this study.

579 CONCLUSIONS

580 A sapphirine-bearing Al-rich chondrule (SARC) was observed in the DaG 978
581 ungrouped type 3 carbonaceous chondrite. Petrographic, mineralogical, and SIMS oxygen
582 isotope and REE geochemical analyses were conducted and the following conclusions were
583 drawn:

- 584 1) The ^{16}O -rich spinel and olivine in the SARC are of relict origin.
- 585 2) The high bulk Al_2O_3 contents, the presence of relict spinel, and the characteristic
586 Group II REE composition in mesostasis strongly indicate that the precursor of the
587 Al-rich portion of the SARC is a mixture of materials from CAIs and ferromagnesian
588 chondrules.
- 589 3) The Al-rich portion of the SARC experienced melt-gas oxygen isotope exchange in
590 the chondrule-forming region, which could well explain why the oxygen isotopic
591 compositions of most Al-rich chondrules are similar to those of ferromagnesian
592 chondrules.
- 593 4) The presence of ^{16}O -rich olivine indicates that AOA's contributed in some manner to
594 the formation of ferromagnesian chondrules.

595 5) After accretion onto the parent body of DaG 978, components in the SARC
596 experienced oxygen and Fe-Mg exchange to various degrees, likely during fluid-
597 assisted thermal metamorphism.

598 **ACKNOWLEDGEMENTS**

599 We thank Dr. Shogo Tachibana for constructive discussion. We are grateful to the critical
600 and helpful comments by Dr. Yunbin Guan, Dr. Travis Tenner, an anonymous reviewer, and
601 Associate Editor Prof. Sara Russell. This study is supported by a Monkasho grant to H.
602 Yurimoto, research grants (Nos. 41073052 and 41373065) from the National Science
603 Foundation of China (NSFC) and a Fellowship Grant-in-Aid from the Japan Society for the
604 Promotion of Science (JSPS) to A.C. Zhang.

605 **REFERENCES**

- 606 Akaki T., Nakamura T., Noguchi T. and Tsuchiyama A. (2007) Multiple formation of
607 chondrules in the early solar system: Chronology of a compound Al-rich chondrule. *The*
608 *Astrophysical Journal* **656**, L29–L32.
- 609 Anders E. and Grevesse N. (1989) Abundances of the elements-Meteoritic and solar.
610 *Geochimica et Cosmochimica Acta* **53**, 197–214.
- 611 Bischoff A. and Keil K. (1984) Al-rich objects in ordinary chondrites: Related origin of
612 carbonaceous and ordinary chondrites and their constituents. *Geochimica et*
613 *Cosmochimica Acta* **48**, 693–709.
- 614 Bischoff A., Palme H. and Spettel B. (1989) Al-rich chondrules from the Ybbsitz H4-
615 chondrite: evidence for formation by collision and splashing. *Earth and Planetary*
616 *Science Letters* **93**, 170–180.
- 617 Boynton W. V. (1975) Fractionation in the solar nebula: condensation of yttrium and the rare
618 earth elements. *Geochimica et Cosmochimica Acta* **39**, 569–584.
- 619 Chakraborty S. (2010) Diffusion coefficients in olivine, wadsleyite and ringwoodite. *Reviews*
620 *in Mineralogy & Geochemistry* **72**, 603–639.
- 621 Davis A. M. and Grossman L. (1979) Condensation and fractionation of rare earths in the
622 solar nebula. *Geochimica et Cosmochimica Acta* **43**, 1611–1632.

- 623 Desch S. J., Morris M. A., Connolly H. C. Jr. and Boss A. P. (2012) The importance of
624 experiments: Constrains on chondrule formation models. *Meteoritics & Planetary*
625 *Science* **47**, 1139–1156.
- 626 Dimanov A. and Wiedenbeck M. (2006) (Fe,Mn)-Mg interdiffusion in natural diopside: effect
627 of pO_2 . *European Journal of Mineralogy* **18**, 705–718.
- 628 Elphick S. C., Graham C. M. and Dennis P. F. (1988) An ion microprobe study of anhydrous
629 oxygen diffusion in anorthite: A comparison with hydrothermal data and some
630 geological implications. *Contrib Mineral Petrol* **100**, 490–495.
- 631 Farver J. (1989) Oxygen diffusion in diopside with application to cooling rate determinations.
632 *Earth and Planetary Science Letters* **92**, 386–396.
- 633 Freer R. and O'Reilly W. (1980) The diffusion of Fe^{2+} ions in spinels with relevance to the
634 process of maghemitization. *Mineralogical Magazine* **43**, 889–899.
- 635 Fuchs L. H. (1969) Occurrence of cordierite and aluminous orthoenstatite in the allende
636 meteorite. *The American Mineralogist* **54**, 1645–1653.
- 637 Ganguly J. and Tazzoli V. (1994) Fe^{2+} -Mg interdiffusion in orthopyroxene: Retrieval from the
638 data on intracrystalline exchange reaction. *American Mineralogist* **79**, 930–937.
- 639 Giletti B. J., Semet M. P. and Yund R. A. (1978) Studies in diffusion-III. Oxygen in feldspars:
640 An ion microprobe determination. *Geochimica et Cosmochimica Acta* **42**, 45–57.
- 641 Gounelle M., Krot A. N., Nagashima K. and Kearsley A. (2009) Extreme ^{16}O enrichment in
642 calcium-aluminum-rich inclusions from the Isheyevo (CH/CB) chondrite. *The*
643 *Astrophysical Journal* **698**, L18–L22.
- 644 Guan Y. B., Huss G. R., Leshin L. A., MacPherson G. J. and McKeegan K. D. (2006) Oxygen
645 isotope and ^{26}Al - ^{26}Mg systematics of aluminum-rich chondrules from unequilibrated
646 enstatite chondrites. *Meteoritics & Planetary Science* **41**, 33–47.
- 647 Hallwig D., Schachtner R. and Sockel H. G. (1982) Diffusion of magnesium, silicon and
648 oxygen in Mg_2SiO_4 and formation of the compound in the solid state. *In: Reactivity in*
649 *Solids*. Dyrek K., Habor J., and Nowotry J. (eds) *Proc Intl Symp* (9th). pp166–169.
- 650 Hier-Majumder S., Anderson I. M. and Kohlstedt D. L. (2005) Influence of protons on Fe-Mg
651 interdiffusion in olivine. *Journal of Geophysical Research* **110**:B02202,
652 doi:10.1029/2004JB003292.

- 653 Hiyagon H. and Hashimoto A. (1999) ^{16}O excesses in olivine inclusions in Yamato-86009 and
654 Murchison chondrules and their relation to CAIs. *Science* **283**, 828–831.
- 655 Imai H. and Yurimoto H. (2003) Oxygen isotopic distribution in an amoeboid olivine
656 aggregate from the Allende CV chondrite: Primary and secondary processes. *Geochimica
657 et Cosmochimica Acta* **67**, 765–772.
- 658 Itoh S., Kojima H. and Yurimoto H. (2004) Petrography and oxygen isotopic compositions in
659 refractory inclusions from CO chondrites. *Geochimica et Cosmochimica Acta* **68**, 183–
660 194.
- 661 Itoh S., Russell S. S. and Yurimoto H. (2007) Oxygen and magnesium isotopic compositions
662 of amoeboid olivine aggregates from the Semarkona LL3.0 chondrite. *Meteoritics &
663 Planetary science* **42**, 1241–1247.
- 664 Jaoul O., Houlier B., and Abel F. (1983) Study of ^{18}O diffusion in magnesium orthosilicate by
665 nuclear microanalysis. *Journal of Geophysical Research* **88**, 613–624.
- 666 Jones R. H., Leshin L. A., Guan Y., Sharp Z. D., Durakiewicz T. and Schilk A. J. 2004.
667 Oxygen isotope heterogeneity in chondrules from the Mokoia CV3 carbonaceous
668 chondrite. *Geochimica et Cosmochimica Acta* **68**, 3423–3438.
- 669 Katayama J., Itoh S. and Yurimoto H. (2012) Oxygen isotopic zoning of reversely zoned
670 melilite crystals in a fluffy type A Ca-Al-rich inclusions from the Vigarano meteorite.
671 *Meteorit. Planet. Sci.* **47**, 2094–2106.
- 672 Kawasaki N., Sakamoto N. and Yurimoto H. (2012) Oxygen isotopic and chemical zoning of
673 melilite crystals in a type A Ca-Al-rich inclusion of Efremovka CV3 chondrite. *Meteorit.
674 Planet. Sci.* **47**, 2084–2093.
- 675 Kobayashi S., Imai H. and Yurimoto H. (2003) New extreme ^{16}O -rich reservoir in the early
676 solar system. *Geochem. J.* **37**, 663–669.
- 677 Kohn M. J. (1999) Why most “dry” rocks should cool “wet”. *American Mineralogist* **84**,
678 570–580.
- 679 Komatsu M., Krot A. N., Petaev M. I., Ulyanov A. A., Keil K. and Miyamoto M. (2001)
680 Mineralogy and petrography of amoeboid olivine aggregates from the reduced CV3
681 chondrites Efremovka, Leoville and Vigarano: Products of nebular condensation,
682 accretion and annealing. *Meteoritics & Planetary Science* **36**, 629–641.

- 683 Krot A. N. and Keil K. (2002) Anorthite-rich chondrules in CR and CH carbonaceous
684 chondrites: Genetic link between calcium-aluminum-rich inclusions and ferromagnesian
685 chondrules. *Meteoritics & Planetary Science* **37**, 91–111.
- 686 Krot A. N., Hutcheon I. D. and Keil K. (2002) Plagioclase-rich chondrules in the reduced CV
687 chondrites: Evidence for complex formation history and genetic links between calcium-
688 aluminum-rich inclusions and ferromagnesian chondrules. *Meteoritics & Planetary
689 Science* **37**, 155–182.
- 690 Krot A. N., Yurimoto H., McKeegan K. D., Leshin L., Chaussidon M., Libourel G., Yoshitake
691 M., Huss G. R., Guan Y. and Zanda B. (2006) Oxygen isotopic compositions of
692 chondrules: Implications for evolution of oxygen isotopic reservoirs in the inner solar
693 nebula. *Chemie der Erde* **66**, 249–276.
- 694 Krot A. N., Chaussidon M., Yurimoto H., Sakamoto N., Nagashima K., Hutcheon I. D. and
695 MacPherson G. J. (2008) Oxygen isotopic compositions of Allende Type C CAIs:
696 Evidence for isotopic exchange during nebular melting and asteroidal metamorphism.
697 *Geochimica et Cosmochimica Acta* **72**, 2534–2555.
- 698 MacPherson G. J. and Huss G. R. (2005) Petrogenesis of Al-rich chondrules: Evidence from
699 bulk compositions and phase equilibria. *Geochimica et Cosmochimica Acta* **69**, 3099–
700 3127.
- 701 Maruyama S. and Yurimoto H. (2003) Relationship among O, Mg isotopes and the
702 petrography of two spinel-bearing compound chondrules. *Geochimica et Cosmochimica
703 Acta* **67**, 3943–3957.
- 704 Maruyama S., Yurimoto H. and Sueno S. (1999) Oxygen isotope evidence regarding the
705 formation of spinel-bearing chondrules. *Earth and Planetary Science Letters* **169**, 165–
706 171.
- 707 Misawa K. and Nakamura N. (1988) Highly fractionated rare-earth elements in
708 ferromagnesian chondrules from the Felix (CO3) meteorite. *Nature* **334**, 47–50.
- 709 Nagashima K., Krot A. N. and Huss G. R. (2012) Oxygen-isotope compositions of chondrules
710 and matrix grains in the LEW 87232, Kakangari-like chondrite. 43rd Lunar and Planetary
711 Science Conference. Abstract #1768.
- 712 Onuma N., Higuchi H., Wakita H. and Nagasawa H. (1968) Trace element partition between
713 2 pyroxenes and host lava. *Earth and Planetary Science Letters* **5**, 47–51.

- 714 Palme H., Wlotzka F., Nagel K. and El Goresy A. (1982) An ultra-refractory inclusion from
715 the Ornans carbonaceous chondrite. *Earth and Planetary Science Letters* **61**, 1–12.
- 716 Rubin A. E. (2004) Aluminum low-Ca pyroxene in a Ca-Al-rich chondrule from the
717 Semarkona meteorite. *American Mineralogist* **89**, 867–872.
- 718 Rudraswami N. G., Ushikubo T., Nakashima D. and Kita N. T. (2011) Oxygen isotope
719 systematics of chondrules in the Allende CV3 chondrite: High precision ion microprobe
720 studies. *Geochimica et Cosmochimica Acta* **75**, 7596–7611.
- 721 Russell S. S., MacPherson G. J., Leshin L. A. and McKeegan K. D. (2000) ¹⁶O enrichments in
722 aluminum-rich chondrules from ordinary chondrites. *Earth and Planetary Science
723 Letters* **184**, 57–74.
- 724 Russell S. S., Krot A. N., Huss G. R., Keil K., Itoh S., Yurimoto H. and MacPherson G. J.
725 (2005) The genetic relationship between refractory inclusions and chondrules. In
726 *Chondrites and the Protoplanetary Disk* (eds. A. N. Krot, E. R. D. Scott, and B.
727 Reipurth). ASP Conference Series, vol. 341. Pp. 317–350.
- 728 Ryerson F. J., Durham W. B., Cherniak D.J. and Lanford W.A. (1989) Oxygen diffusion in
729 olivine: Effect of oxygen fugacity and implications for creep. *Journal of Geophysical
730 Research* **94**, 4105–4118.
- 731 Ryerson F. J. and McKeegan K. D. (1994) Determination of oxygen self-diffusion in
732 akermanite, anorthite, diopside, and spinel: Implications for oxygen isotopic anomalies
733 and the thermal histories of Ca-Al-rich inclusions. *Geochimica et Cosmochimica Acta* **58**,
734 3713–3734.
- 735 Sheng Y. J. (1992) Origin of plagioclase-olivine inclusions. Ph.D. thesis, California Institute
736 of Technology, Pasadena, California, USA. Pp 271.
- 737 Sheng Y. J., Hutcheon I. D. and Wasserburg G. J. (1991) Origin of plagioclase-olivine
738 inclusions in carbonaceous chondrites. *Geochimica et Cosmochimica Acta* **55**, 581–599.
- 739 Tenner T. J., Ushikubo T., Kurahashi E., Kita N. T. and Nagahara H. (2013) Oxygen isotope
740 systematics of chondrule phenocrysts from the CO3.0 chondrite Yamato 81020: evidence
741 for two distinct oxygen isotope reservoirs. *Geochim. Cosmochim. Acta* **102**, 226–245.
- 742 Tronche E. J., Hewins R. H. and MacPherson G. J. (2007) Formation conditions of
743 aluminum-rich chondrules. *Geochimica et Cosmochimica Acta* **71**, 3361–3381.

- 744 Ushikubo T., Kimura M., Kita N. T. and Valley J. W. (2012) Primordial oxygen isotope
745 reservoirs of the solar nebula recorded in chondrules in Acfer 094 carbonaceous
746 chondrite. *Geochimica et Cosmochimica Acta* **90**, 242–264.
- 747 Wakaki S., Itoh S., Tanaka T. and Yurimoto H. (2013) Petrology, trace element abundances
748 and oxygen isotopic compositions of a compound CAI-chondrule object from Allende.
749 *Geochimica et Cosmochimica Acta* **102**, 261–279.
- 750 Wang W. Y. and Yurimoto H. (1993) Analysis of rare earth elements in garnet by SIMS. *Ann.*
751 *Rep. Inst. Geosci., Univ. Tsukuba* **19**, 87–91.
- 752 Wasson J. T., Yurimoto H. and Russell S. S. (2001) ^{16}O -rich melilite in CO3.0 chondrites:
753 Possible formation of common, ^{16}O -poor melilite by aqueous alteration. *Geochimica et*
754 *Cosmochimica Acta* **65**, 4539–4549.
- 755 Yasuda M., Kitamura M. and Morimoto N. (1983) Electron microscopy of clinoenstatite from
756 boninite and a chondrite. *Physics and Chemistry of Minerals* **9**, 192–196.
- 757 Yu Y., Hewins R. H., Clayton R. N. and Mayeda T. K. (1995) Experimental study of high
758 temperature oxygen isotope exchange during chondrule formation. *Geochimica et*
759 *Cosmochimica Acta* **59**, 2095–2104.
- 760 Yurimoto H. and Wasson J. T. (2002) Extremely rapid cooling of a carbonaceous-chondrite
761 chondrule containing very ^{16}O -rich olivine and a ^{26}Mg -excess. *Geochimica et*
762 *Cosmochimica Acta* **66**, 4355–4363.
- 763 Yurimoto H., Krot A. N., Choi B.-G., Aleon J., Kunihiro T. and Brearley A.J. (2008) Oxygen
764 isotopes of chondritic components. *Reviews in Mineralogy & Geochemistry* **68**, 141–186.
- 765 Yurimoto H., Nagasawa H., Mori Y. and Matsubaya O. (1994) Microdistribution of oxygen
766 isotopes in a refractory inclusion from the Allende meteorite. *Earth and Planetary*
767 *Science Letters* **128**, 47–53.
- 768 Yurimoto H., Yamashita A., Nishida N. and Sueno S. (1989) Quantitative SIMS analysis of
769 GSJ rock reference samples. *Geochemical Journal* **23**, 215–236.
- 770 Zhang A. C. and Hsu W. B. (2009) Refractory inclusions and aluminum-rich chondrules in
771 Sayh Al Uhaymir 290 CH chondrite: Petrography and Mineralogy. *Meteoritics &*
772 *Planetary Science* **44**, 787–804.

- 773 Zhang A. C., Itoh S., Yurimoto H., Sun Q. and Wang R. C. (2011) Formation of the
774 Sapphirine-bearing Al-rich Chondrule in the DaG 978 Carbonaceous Chondrite:
775 Preliminary Mineralogical and Oxygen Isotopic Results. Workshop for formation of the
776 First Solids in the Solar System, abstract #9028.
- 777 Zhang A. C. and Yurimoto H. (2013) Petrography and mineralogy of the ungrouped type 3
778 carbonaceous chondrite Dar al Gani 978. *Meteoritics & Planetary Science* **48**, 1651–
779 1677.
- 780 Zhang A. C., Itoh S, Sakamoto N, Wang R. C. and Yurimoto H. (2013) Heterogeneous
781 oxygen isotopic compositions in a sapphirine-bearing Al-rich chondrule from the DaG
782 978 carbonaceous chondrite. 44th Lunar and Planetary Science Conference, abstract
783 #1449.
- 784

Figure Captions

785

786 Figure 1. Back-scattered electron (BSE) image of the sapphirine-bearing Al-rich chondrule in
787 DaG 978. The dashed and solid lines indicate the core-mantle and mantle-rim boundaries,
788 respectively.

789 Figure 2. BSE images of the core in the SARC. (a) Small spinel grains are included in
790 anorthite, Al-rich enstatite, and sapphirine. (b) Euhedral sapphirine grains are randomly
791 distributed in mesostasis.

792 Figure 3. BSE images of the mantle in the SARC. (a) Typical area in the mantle, which
793 contains euhedral anorthite, enstatite, and mesostasis. (b) Transition zone between the core
794 and mantle, distinguished by the presence or lack of spinel, respectively. (c) Augite grain in
795 mesostasis up to 20 μm in size and the Fe-rich, low-Al enstatite in mesostasis is
796 approximately 5 μm thick. (d) Several anhedral olivine grains and FeNi metal in the mantle.

797 Figure 4. BSE images of the SARC rim, which mainly contains of Fe-rich olivine, enstatite,
798 and FeNi metal. Al-en: Al-rich enstatite; an: anorthite; meso: mesostasis; sp: spinel; spr:
799 sapphirine; en: enstatite; ol: olivine.

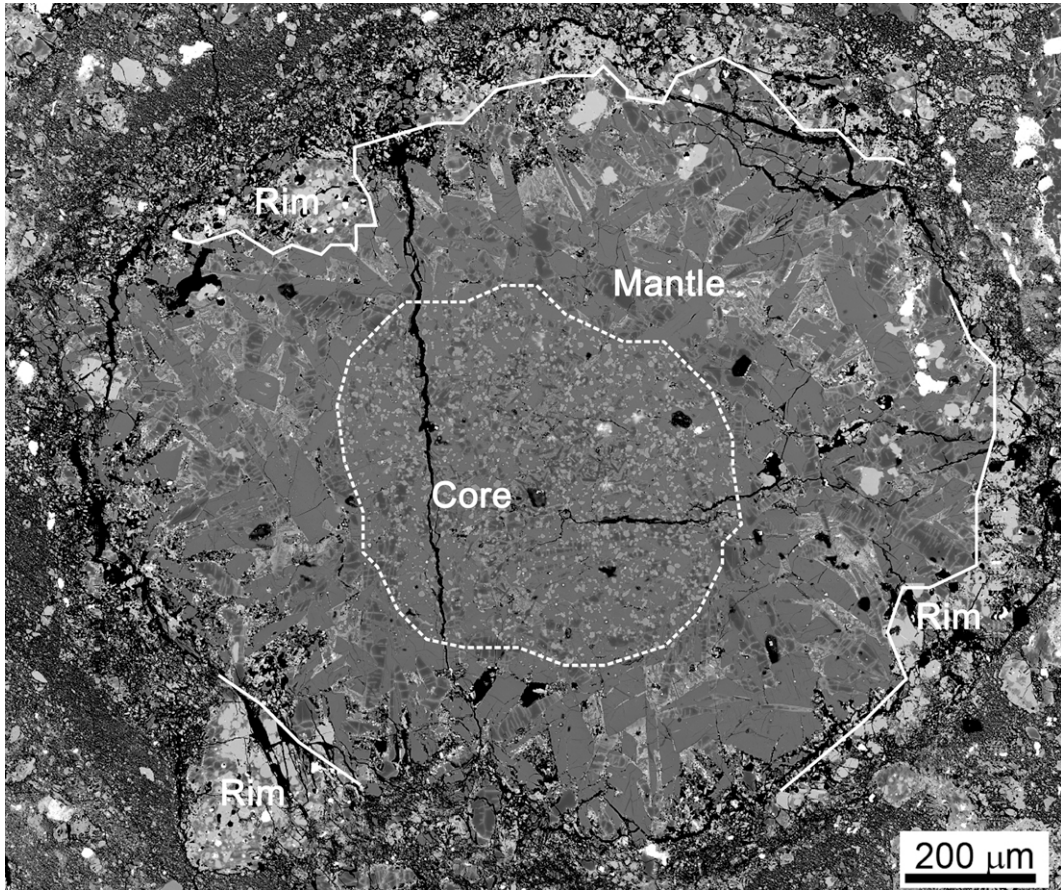
800 Figure 5. Oxygen isotopic compositions of minerals and mesostasis presented on oxygen
801 three-isotope diagrams. Error bars denote two standard deviation (2σ). En: enstatite; an:
802 anorthite; meso: mesostasis; sp: spinel; spr: sapphirine; ol: olivine.

803 Figure 6. REE pattern of mesostasis in the SARC from DaG 978. Error bars denote one
804 standard deviation (1σ).

805 Figure 7. Curves showing diffusion time as a function of temperature for various diffusion
806 lengths. Solid curves represent minimum temperatures and diffusion times for the estimated
807 oxygen and Fe-Mg diffusion lengths observed in this study. Dashed lines represent the upper
808 limits of temperature and diffusion time, based on estimated upper limits of O diffusion
809 lengths in olivine and spinel. (a) Under anhydrous conditions. The diffusion coefficients for
810 oxygen in spinel, anorthite, forsterite, and diopside under anhydrous conditions are from
811 Ryerson and McKeegan (1994), Elphick et al. (1988), and Hallwig et al. (1982). The
812 diffusion coefficients for Fe-Mg in spinel, forsterite, Al-poor enstatite, and diopside under
813 anhydrous conditions are from Freer and O'Reilly (1980), Ganguly and Tazzoli (1994),
814 Dimanov and Wiedenbeck (2006), and Chakraborty (2010). (b) Under hydrous conditions.
815 The diffusion coefficients for oxygen in anorthite, forsterite, and diopside under hydrous
816 conditions are from Giletti et al. (1978), Jaoul et al. (1983), and Farver (1989).

817 Figure 8. Schematic diagram for the formation of SARC in DaG 978. Diamond and rectangle
818 symbols represent spinel and olivine, respectively.

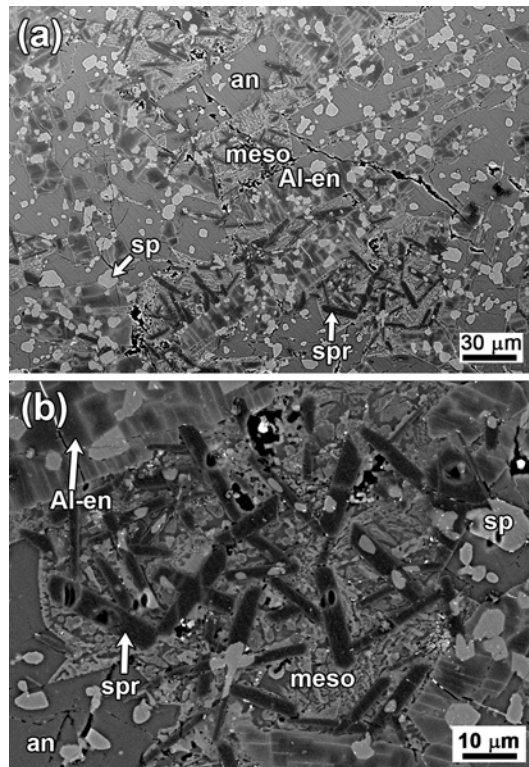
819



820

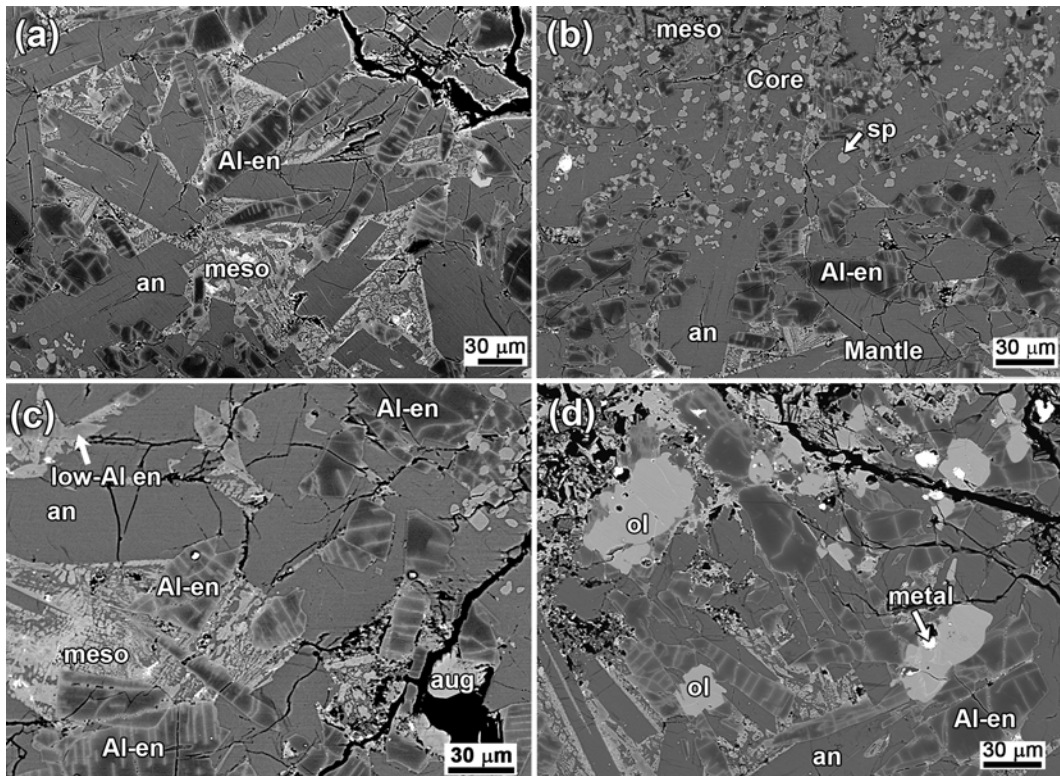
821 Figure 1.

822

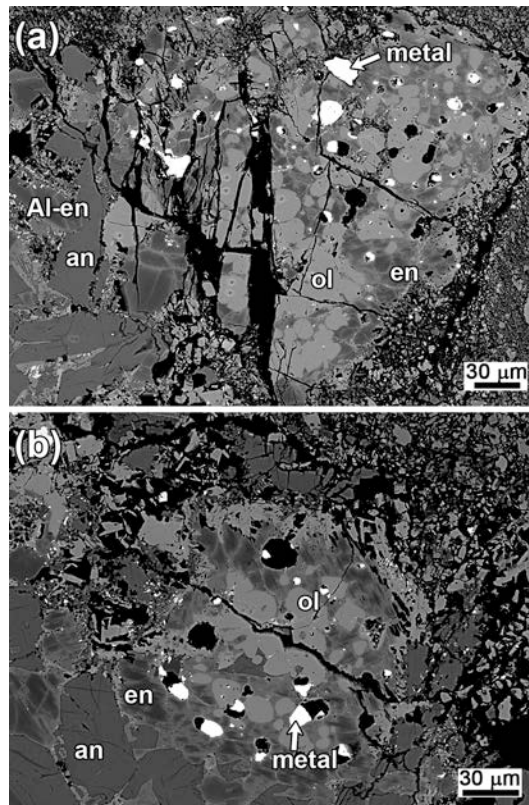


823
824
825

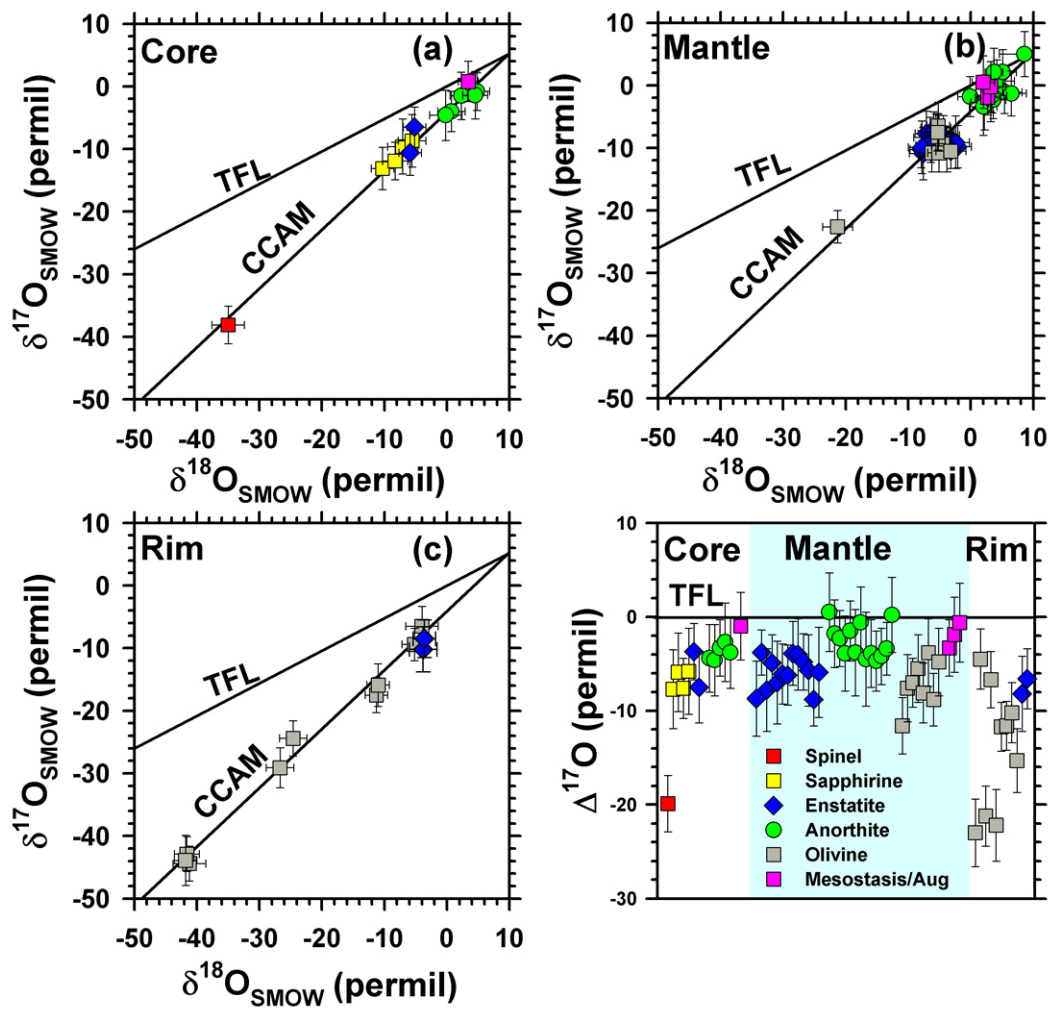
Figure 2.



826
827 Figure 3
828



829
830 Figure 4
831
832

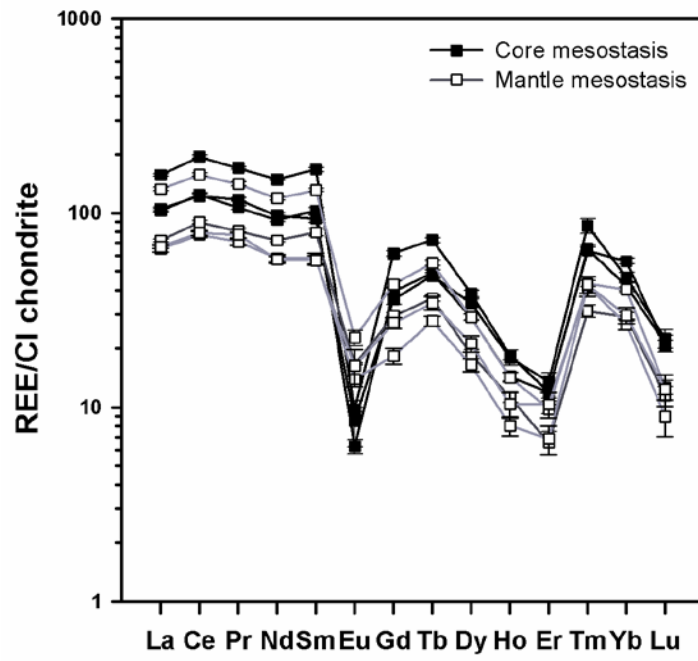


833

834 Figure 5.

835

836

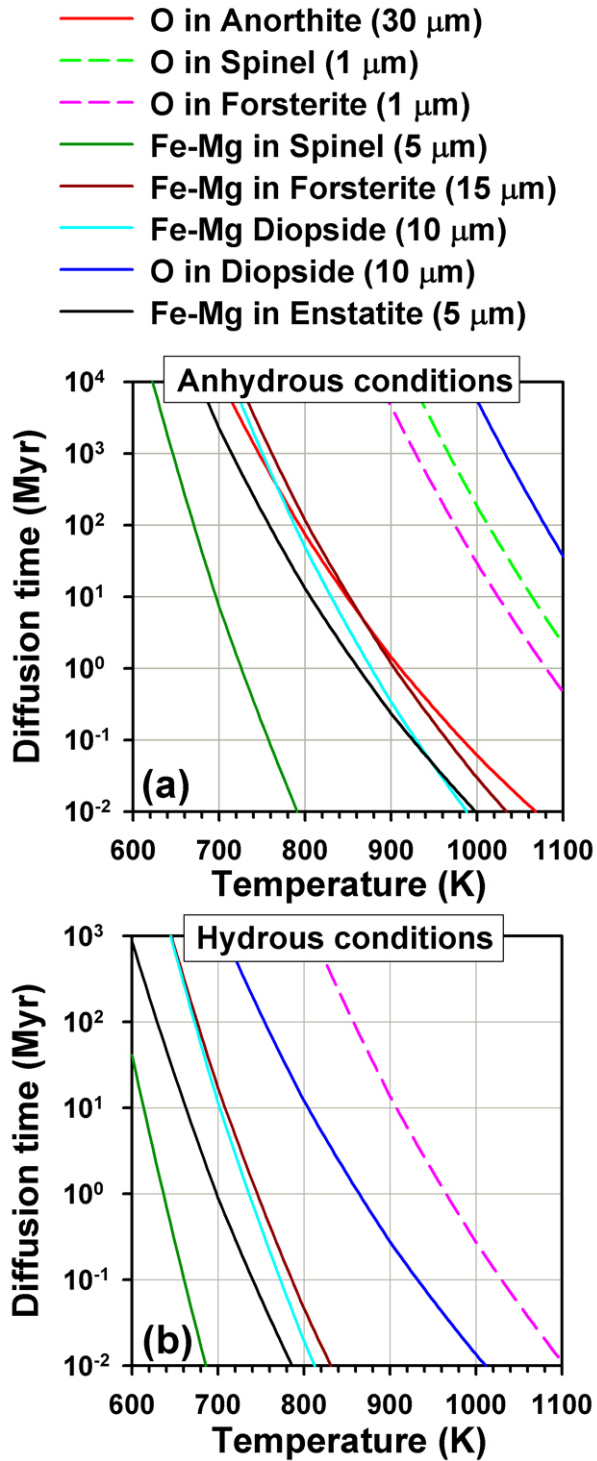


837

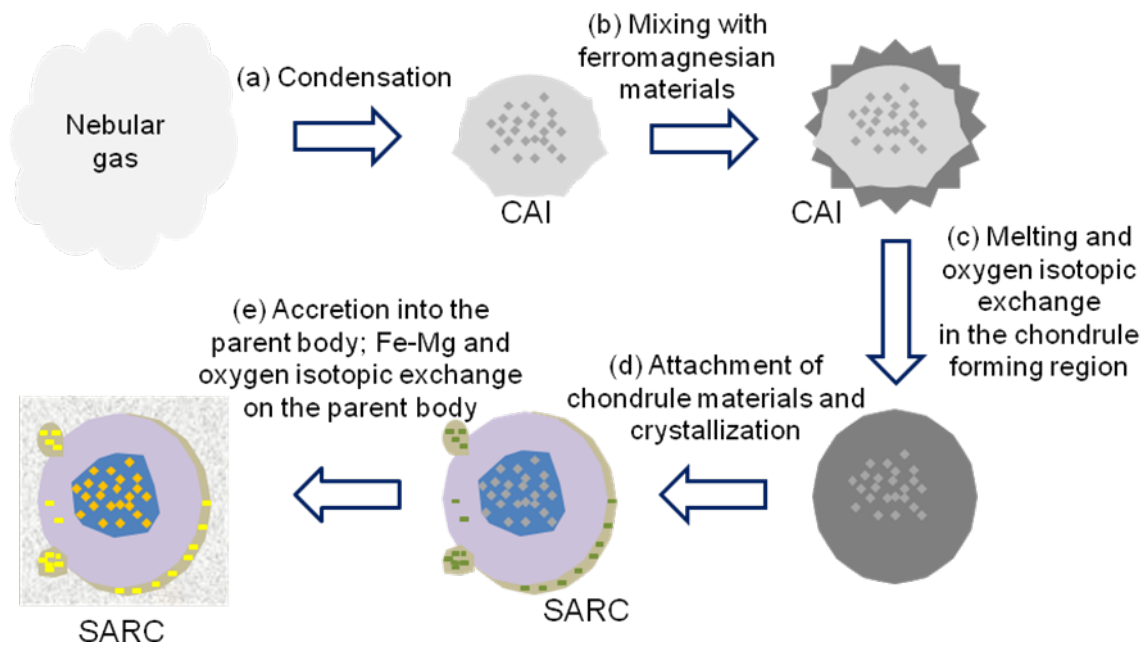
838 Figure 6.

839

840



841
 842 Figure 7.
 843



844

845 Figure 8.

846

847

848

849 Table 1. Representative chemical compositions (wt%) of minerals in SARC from DaG 978

	Core minerals				Mantle minerals						Rim minerals		
	sp	spr	an	en	an	an	en	en	en	ol	aug	ol	en
SiO ₂	0.14	17.9	45.9	51.1	45.0	46.9	51.2	52.0	54.3	38.2	50.9	36.9	56.0
TiO ₂	0.34	1.44	0.06	1.57	0.04	0.06	1.57	1.07	1.63	0.06	0.14	0.08	0.18
Al ₂ O ₃	65.1	54.9	34.9	10.9	35.1	33.5	10.5	3.71	4.91	bd	0.43	0.02	1.08
Cr ₂ O ₃	1.34	1.09	bd	0.25	0.03	bd	0.34	0.28	0.47	bd	0.05	bd	0.16
MgO	14.6	23.7	bd	34.6	bd	0.18	32.8	28.4	37.3	34.9	11.2	34.4	36.8
MnO	0.12	0.08	0.02	0.07	bd	bd	0.11	0.26	0.24	0.28	0.11	0.39	0.07
FeO	18.0	0.40	0.21	0.37	0.23	0.31	0.37	14.0	0.73	25.8	11.3	27.7	4.64
CaO	0.10	0.16	18.1	0.68	18.1	17.2	0.74	0.74	0.69	0.05	25.1	bd	0.52
Na ₂ O	bd	bd	1.55	0.02	1.54	2.13	bd	0.04	0.03	bd	0.12	bd	bd
Total	99.7	99.7	100.8	99.6	100.0	100.2	97.5	100.5	100.3	99.3	99.4	99.5	99.4
Calculated based on 24 oxygen atoms													
Si	0.022	2.494	6.311	6.925	6.239	6.468	7.059	7.437	7.330	6.086	7.823	5.945	7.722
Ti	0.040	0.150	0.006	0.160	0.004	0.006	0.162	0.115	0.165	0.007	0.016	0.010	0.019
Al	11.907	8.999	5.645	1.738	5.725	5.435	1.703	0.624	0.780	bd	0.078	0.004	0.175
Cr	0.164	0.120	bd	0.027	0.003	bd	0.037	0.032	0.050	bd	0.006	bd	0.017
Mg	3.405	4.953	bd	7.033	bd	0.037	6.783	6.093	7.552	8.341	2.582	8.313	7.612
Mn	0.016	0.009	0.002	0.008	bd	bd	0.013	0.031	0.027	0.038	0.014	0.053	0.008
Fe	2.332	0.046	0.024	0.042	0.027	0.036	0.043	1.669	0.082	3.426	1.447	3.719	0.533
Ca	0.017	0.024	2.666	0.099	2.689	2.541	0.109	0.113	0.100	0.009	4.133	bd	0.077
Na	bd	bd	0.412	0.005	0.413	0.569	bd	0.011	0.008	bd	0.036	bd	bd

850 Bd: below detection limit. Sp: spinel; spr: sapphirine; an: anorthite; en: enstatite; ol: olivine;
851 aug: augite.

852

853

854 Table 2. SEM-EDS bulk compositions (wt%) of the core and mantle and their respective
 855 mesostasis in SARC

	Core		Mantle	
	Bulk	Mesostasis	Bulk	Mesostasis
Na ₂ O	1.1	1.1	1.8	1.7
MgO	13.0	14.2	10.6	6.4
Al ₂ O ₃	29.3	27.2	21.6	14.6
SiO ₂	40.8	40.9	48.8	53.0
CaO	8.8	8.9	11.5	16.3
TiO ₂	0.9	1.6	0.9	1.3
Cr ₂ O ₃	0.9	1.4	0.3	0.1
FeO	5.4	4.6	4.5	6.6
Total	100	100	100	100

856

857

858 Table 3. Oxygen isotopic compositions (permil) of minerals and mesostasis in SARC

	$\delta^{18}\text{O}_{\text{SMOW}}$	2σ	$\delta^{17}\text{O}_{\text{SMOW}}$	2σ	$\Delta^{17}\text{O}$	2σ
Core minerals and mesostasis						
<i>Spinel</i>						
dag@70	-35.0	2.6	-38.1	3.0	-19.9	3.0
<i>Sapphirine</i>						
dag@71	-7.1	2.4	-9.6	4.4	-5.9	4.2
dag@74	-10.3	1.8	-13.1	3.4	-7.7	4.2
dag@115	-8.3	2.0	-11.9	3.0	-7.6	3.2
dag@116	-5.6	2.2	-8.7	4.2	-5.8	4.6
<i>Enstatite</i>						
dag@113	-5.2	1.8	-6.5	3.2	-3.7	3.0
dag@120	-5.9	1.8	-10.6	3.6	-7.5	3.8
<i>Anorthite</i>						
dag@107	-0.7	2.0	-3.4	3.8	-3.1	3.8
dag@108	0.7	2.2	-4.0	3.2	-4.4	3.6
dag@110	-0.2	2.6	-4.6	4.0	-4.6	3.8
dag@111	4.8	2.0	-0.8	3.0	-3.3	3.0
dag@112	2.3	1.8	-1.5	3.8	-2.7	4.2
dag@118	4.5	2.0	-1.4	3.8	-3.8	3.8
<i>Mesostasis</i>						
dag@122	-2.9	1.6	-5.7	4.6	-4.2	4.8
dag@125	3.4	1.6	0.8	3.2	-1.0	3.6

859

860

	$\delta^{18}\text{O}_{\text{SMOW}}$	2σ	$\delta^{17}\text{O}_{\text{SMOW}}$	2σ	$\Delta^{17}\text{O}$	2σ
Mantle minerals and mesostasis						
<i>Enstatite</i>						
dag@35	-2.1	2.2	-9.8	3.4	-8.7	4.0
dag@36	-5.6	2.4	-6.8	2.2	-3.8	2.4
dag@38	-2.4	2.2	-9.1	4.2	-7.8	4.4
dag@42	-6.5	2.6	-8.3	3.2	-4.9	3.0
dag@50	-7.6	2.2	-10.9	4.2	-7.0	4.4
dag@52	-7.9	1.8	-10.2	3.0	-6.1	3.2
dag@55	-6.4	2.4	-9.5	2.8	-6.2	3.2
dag@90	-5.9	2.0	-7.0	2.8	-3.9	3.4
dag@91	-7.1	1.8	-7.7	3.6	-4.0	3.8
dag@93	-5.1	2.2	-7.4	2.6	-4.8	3.0
dag@99	-4.4	2.6	-8.0	3.2	-5.7	3.8
dag@142	-3.2	2.4	-10.5	2.8	-8.8	2.8
dag@143	-7.8	2.2	-9.9	4.2	-5.9	4.8
<i>Anorthite</i>						
dag@33	4.4	2.6	-1.1	4.8	-3.4	5.0
dag@34	8.6	4.0	5.0	3.6	0.5	4.2
dag@40	-0.1	2.0	-1.8	3.2	-1.8	3.6
dag@41	3.6	1.8	-0.4	3.0	-2.3	3.0
<i>Anorthite#1</i>						
dag@87#1	5.4	2.8	-1.1	3.4	-3.9	4.0
dag@88#1	4.2	2.8	0.7	3.4	-1.5	3.2
dag@89	2.2	2.2	-2.7	4.4	-3.8	4.6
dag@92	5.1	2.2	2.1	3.6	-0.6	3.8
dag@94	2.0	2.2	-3.4	4.6	-4.5	5.0
dag@97	3.2	2.2	-2.2	3.6	-3.9	3.6
dag@98	6.5	2.4	-1.3	3.6	-4.7	3.2
dag@119	3.6	2.0	-2.3	3.0	-4.2	3.0
dag@138	3.4	2.4	-1.6	2.8	-3.4	2.8
dag@139	3.7	1.4	2.1	3.8	0.2	4.0
<i>Olivine</i>						
dag@45	-7.5	2.2	-12.3	3.4	-8.5	3.6
<i>Olivine#1</i>						
dag@46	-21.3	2.4	-22.6	2.6	-11.6	3.0
dag@49	-5.2	2.2	-8.2	3.6	-5.5	3.6
dag@51	-5.1	1.8	-10.8	3.0	-8.1	3.2
dag@47	-6.2	2.0	-10.8	3.0	-7.6	3.6
dag@48	-4.5	1.8	-9.4	2.4	-7.0	2.6
dag@140	-5.2	1.8	-6.5	3.8	-3.8	3.6
dag@141	-3.2	2.4	-10.5	2.8	-8.8	2.8
dag@144	-5.3	2.6	-7.5	3.0	-4.8	3.6
<i>Mesostasis</i>						
dag@95(aug)	5.2	2.8	-0.3	3.4	-2.9	3.6
dag@104	2.7	2.0	-1.9	2.8	-3.3	3.0
dag@105	3.2	2.4	-0.2	4.0	-1.9	4.0
dag@106	2.0	1.8	0.5	4.2	-0.6	4.2

863 Table 3. continued

	$\delta^{18}\text{O}_{\text{SMOW}}$	2σ	$\delta^{17}\text{O}_{\text{SMOW}}$	2σ	$\Delta^{17}\text{O}$	2σ
Rim minerals						
<i>Olivine</i>						
dag@56	-11.4	1.8	-14.7	3.0	-8.8	3.0
<i>Olivine#2</i>						
dag@57	-41.2	2.6	-44.4	2.8	-23.0	3.6
dag@62	-41.6	2.0	-42.9	2.8	-21.2	3.2
dag@131	-41.8	1.8	-43.9	4.0	-22.2	3.8
dag@59	-4.0	2.6	-6.5	3.2	-4.5	3.2
dag@129	-5.2	2.0	-9.4	2.6	-6.7	3.0
<i>Olivine#3</i>						
dag@132	-11.3	1.8	-17.5	2.8	-11.7	2.6
dag@133	-24.6	2.2	-24.4	2.8	-11.6	2.6
dag@135	-26.7	2.2	-29.1	3.2	-15.3	3.4
dag@134	-11.0	1.8	-15.9	3.4	-10.2	3.2
<i>Enstatite</i>						
dag@130	-3.8	2.2	-10.2	3.6	-8.2	4.0
dag@136	-3.6	1.8	-8.5	3.0	-6.6	3.2

864 Individual measurements are from different grains except anorthite grain#1 and olivine grains #1, #2,
865 and #3. Intra-grain heterogeneities are observed in olivine grains #1 and #3.

866

867 Table 4. REE concentrations (ppm) in the core and mantle mesostasis of SARC

	Core mesostasis								Mantle mesostasis							
	c-1	1 σ	c-2	1 σ	c-3	1 σ	c-4	1 σ	m-1	1 σ	m-2	1 σ	m-3	1 σ	m-4	1 σ
La	24.6	0.6	24.0	0.5	36.8	0.7	24.1	0.6	15.4	0.6	15.7	0.4	16.9	0.3	31.1	0.6
Ce	73.8	1.6	70.9	0.9	117.2	1.9	74.7	1.8	46.7	1.5	47.6	1.5	54.0	1.0	94.9	2.0
Pr	10.4	0.2	10.4	0.3	15.2	0.3	9.5	0.2	6.3	0.2	6.9	0.2	7.2	0.2	12.6	0.3
Nd	43.9	1.3	40.8	0.9	67.4	1.1	41.7	1.0	26.4	1.2	26.0	1.0	32.7	0.6	53.8	1.2
Sm	13.7	0.6	12.5	0.4	24.6	0.6	15.0	0.6	8.6	0.5	8.4	0.5	11.7	0.5	19.3	0.4
Eu	0.5	0.1	0.9	0.3	0.5	0.1	0.4	0.1	0.8	0.0	0.9	0.2	0.9	0.1	1.3	0.1
Gd	7.1	0.4	7.7	0.5	12.1	0.4	7.7	0.3	3.6	0.3	5.3	0.3	5.8	0.2	8.4	0.3
Tb	1.7	0.1	1.7	0.1	2.6	0.1	1.8	0.1	1.0	0.1	1.2	0.1	1.3	0.0	2.0	0.1
Dy	8.3	0.4	6.6	0.5	9.3	0.4	7.0	0.3	4.0	0.3	5.2	0.5	4.5	0.3	7.1	0.2
Ho	1.0	0.1	0.8	0.1	1.0	0.1	0.8	0.0	0.4	0.1	0.6	0.1	0.6	0.0	0.8	0.0
Er	2.1	0.2	2.2	0.4	1.9	0.1	1.9	0.2	1.1	0.2	1.6	0.2	1.0	0.1	1.6	0.1
Tm	2.1	0.2	1.9	0.2	1.6	0.1	1.6	0.1	1.0	0.1	1.0	0.1	0.8	0.1	1.0	0.0
Yb	7.5	0.5	7.0	0.4	9.2	0.3	6.8	0.4	4.3	0.3	4.8	0.5	4.7	0.3	6.5	0.2
Lu	0.5	0.1	0.4	0.1	0.5	0.1	0.5	0.1	0.2	0.0	0.3	0.1	0.3	0.1	0.3	0.1

868